HHS Public Access

Author manuscript

Mamm Genome. Author manuscript; available in PMC 2024 November 27.

Published in final edited form as:

Mamm Genome. 2023 September ; 34(3): 453–463. doi:10.1007/s00335-023-09999-8.

The spontaneous mouse mutant low set ears (*Lse*) is caused by tandem duplication of *Fgf3* and *Fgf4*

Alana Luzzio[1,*], **Sarah Edie**[1,*], **Kristina Palmer**[1], **L. Brianna Caddle**[1], **Rachel Urban**[1], **Leslie O. Goodwin**[1], **Ian C. Welsh**[1], **Laura G. Reinholdt**[1], **David E. Bergstrom**[1], **Timothy C. Cox**[2], **Leah Rae Donahue**[1], **Stephen A. Murray**[1,#]

[1]The Jackson Laboratory, Bar Harbor, ME USA

[2]Departments of Oral & Craniofacial Sciences and Pediatrics, University of Missouri-Kansas City, Kansas City, MO USA

Abstract

The external ear develops from an organized convergence of ventrally migrating neural crest cells into the first and second branchial arches. Defects in external ear position are often symptomatic of complex syndromes such as Apert, Treacher-Collins, and Crouzon Syndrome. The low set ears (*Lse*) spontaneous mouse mutant is characterized by the dominant inheritance of a ventrally shifted external ear position and an abnormal external auditory meatus (EAM). We identified the causative mutation as a 148Kb tandem duplication on Chromosome 7, which includes the entire coding sequences of *Fgf3* and *Fgf4*. Duplications of *FGF3* and *FGF4* occur in 11q duplication syndrome in humans and are associated with craniofacial anomalies, among other features. Intercrosses of *Lse* affected mice revealed perinatal lethality in homozygotes, and *Lse/Lse* embryos display additional phenotypes including polydactyly, abnormal eye morphology, and cleft secondary palate. The duplication results in increased *Fgf3* and *Fgf4* expression in the branchial arches and additional discrete domains in the developing embryo. This ectopic overexpression resulted in functional FGF signaling, demonstrated by increased *Spry2* and *Etv5* expression in overlapping domains of the developing arches. Finally, a genetic interaction between *Fgf3/4* overexpression and *Twist1*, a regulator of skull suture development, resulted in perinatal lethality, cleft palate and polydactyly in compound heterozygotes. These data indicate a role for *Fgf3* and *Fgf4* in external ear and palate development and provide a novel mouse model for further interrogation of the biological consequences of human *FGF3/4* duplication.

Keywords

structural variation; craniofacial development; FGF signaling; spontaneous mutation

[#]Correspondence: steve.murray@jax.org.
[*]Equal contribution

Competing Interests: The corresponding author, Stephen A. Murray, is an editor-in-chief of the journal. There are no other competing interests.

Introduction

Abnormal external ear phenotypes are often associated with complex human conditions including 11q Duplication (Yelavarthi and Zunich, 2004; Zarate et al., 2007), Treacher-Collins (Dixon, 1995), Okihiro (Kohlhase et al., 2002), and DiGeorge/Velo-cardio-facial/ 22q11 deletion (22q11DS) (Arnold et al., 2006), Crouzon (Lambert and Dodson, 1996), and Oculo-auriculo-vertebral (Tingaud-Sequeira et al., 2022) Syndromes. In these conditions, external ear phenotypes present along a spectrum of degree of severity and illustrate the complexity of interacting pathways that regulate mammalian ear development. Development of the external ear requires orchestrated interaction of migrating cranial neural crest cells, ectodermal and endodermal components of the first and second branchial arches, and the corresponding branchial cleft (Cox et al., 2014; Fekete, 1999; Grevellec and Tucker, 2010; Lambert and Dodson, 1996). Six auricular hillocks, known as the “Hillocks of His”, arise from the first and second brachial arches and develop into the auricular structures which comprise the outer ear: the pinna, tragus, and external auditory meatus (EAM) (Cox et al., 2014; Tekin et al., 2008; Wilkinson et al., 1988). The hillocks of the second branchial arch give rise to most of the pinna while those of the first arch give rise to the tragus (Cox et al., 2014; Mallo 2003). Invagination of the epithelium of the first branchial arch forms the EAM and extends ventrally towards the tympanic ring in response to signaling cues (Fuchs and Tucker, 2015; Minoux et al., 2013). The EAM and the pinna work together as a funnel to channel sound waves to the middle ear via the tympanic membrane, which is supported by the tympanic ring, and ultimately transmits auditory signals to the middle and inner ear (Fuchs and Tucker, 2015). Mouse models have helped define the signaling components involved in the initial invagination and EAM formation. *Goosecoid* knockout mice ($Gsc^{-/-}$) lack a tympanic ring and invagination thus fails to form an EAM. *Homeobox A2* knockout mice ($HoxA2^{-/-}$) develop two tympanic rings and a double EAM (Fuchs and Tucker, 2015; Minoux et al., 2013).

Fibroblast growth factors (FGFs) regulate neural crest induction and migration and are critical for craniofacial morphogenesis (Stanier and Pauws, 2012). The FGF signaling pathway is highly conserved and plays essential roles in cellular proliferation, migration, branching morphogenesis, and cell survival, evoking distinct cellular responses depending on the cellular context and ligand/receptor combination (Brewer et al., 2016; Ornitz and Itoh, 2015; Turner and Grose, 2010; Welsh et al., 2007) . Mutations in *Fgf10* lead to abnormalities in pinna extension and a range of craniofacial abnormalities including cleft palate (Rice et al., 2004; Zhang et al., 2020). *Fgf3* and *Fgf10* are required for proper otic placode induction which ultimately gives rise to the inner ear, including all the specialized sensory neurons and supporting cells (Wright and Mansour, 2003). Moreover, the FGF pathway targets and inhibitors, *Spry1* and *Spry2*, regulate the size of the otic placode (Mahoney Rogers et al., 2011). Together, these data illustrate the complex interaction of pathways which direct craniofacial development, and their sensitivity to perturbations and dosage effects.

Spontaneous mouse mutants provide a unique, phenotype-driven approach for elucidating the complex genetic regulation of craniofacial development, and are useful models of human disease. The low set ears (*Lse*) mutant first arose in 1983 as a spontaneous mutant with

ventrally shifted external ears, adult-onset corneal opacity, bulging eyes, and homozygous embryonic lethality (Theiler and Sweet, 1986). In this study we identify the causative mutation for this line, establish its effect on FGF signaling, and characterize the associated adult and embryonic phenotypes.

Materials and Methods

Animals and husbandry

Lse mutant mice (B6C3Fe a/a-*Lse*/J; JAX STOCK #001280) were maintained by outcrossing to B6C3F1 (STOCK #100010) acquired from JAX Production colonies. For early analysis prior to the identification of the duplication, mice were crossed to CAST/EiJ and embryos genotyped via the polymorphic D7Nds4 marker. *Twist1* mutant mice (B6.129S7-*Twist1*^{tm1Bhr}/J; STOCK #002222) were recovered from cryopreservation and maintained by breeding to C57BL/6J (JAX STOCK #000664), and genotyped using the recommended assays. For timed matings, embryonic day (E) 0.5 was defined as noon on the day a copulation plug was observed after overnight mating. All procedures were reviewed and approved by The Jackson Laboratory Institutional Animal Care and Use Committee and were in accordance with The National Institutes of Health guidelines for the care and use of animals in research.

High-throughput sequencing

Sequencing was performed following array-based capture using a custom Agilent array designed to include the 4.75Mb of sequence (Chr7: 147.5Mb-152.5Mb) surrounding the D7Nds4 marker. An Illumina paired-end libraries from array-enriched *Lse*/+ DNA sample was sequenced on an Illumina GAIIx sequencer and processed as previously described (Fairfield et al., 2015). The *Lse* duplication breakpoint was confirmed by PCR and Sanger sequencing.

Droplet digital PCR (ddPCR)

ddPCR was performed using the QX200 droplet digital system (Bio-Rad). Probes and primers for the *Lse* breakpoint (forward primer: CACAGAAAGGTTGTGAGAGAGTGTGT; reverse primer: GCCACTGTTCTGAGGTGTAATATCA; probe: TGTGTGATATACAGATTTC), genomic *Fgf3* (forward primer: CTGTCTCACAGGATCACTACAAC; reverse primer: AGGCGGGAAGCATATGTATTG; probe: TCCGTTCCACAAACTCACACTCTGC), and genomic Fgf4 (forward primer: AGGTCTTCTGGAGCTCTCTC; reverse primer: GCTCATGGCCACGAAGAA; probe: TGGTGAGCATCTTCGGAGTGGC). Assays and primers were purchased from Integrated DNA Technologies. After the PCR assays were finished, the copy numbers were automatically analyzed using Quanta SoftVersion1.6.6 (Bio Rad, USA). The absolute copy numbers per panel were estimated according to the number of positive wells and the total number of partitions.

Adult skull microCT

Skulls for microCT (11 *Lse*/+ [5 male, 6 female] and 14 +/+ [8 male, 6 female]) were collected and frozen at −20C until imaging. Skulls were then thawed and imaged with a

Skyscan 1076 microCT scanner (Bruker BioSpin Corporation, 15 Fortune Drive, Billerica, MA). Scanning was performed at an isotropic resolution of 34.42 um with the following settings: 55 kV, 180 uA, Al 0.5mm filter, 180 degree scanning, 0.7 degree rotation step, and a 160ms exposure with 3 frame averaging. Raw scan data were reconstructed using NRecon software (V1.6.9.4; Bruker BioSpin Corporation, 15 Fortune Drive, Billerica, MA) with smoothing set to 1. Reconstructed data were rendered and assessed in 3D using Drishti Volume Exploration software (V2.6; http://sf.anu.edu.au/Vizlab/drishti).

Embryo microCT

MicroCT was performed on E18.5 embryos as previously described (Dickinson et al., 2016). Embryos were fixed in 4% PFA, and then equilibrated with stability solution (Wong et al., 2013) for 4 days. The stability buffer was polymerized by 37C incubation for ~3h. Gel was carefully removed with forceps and embryos were incubated in Lugol solution (Sigma-Aldrich Cat# L6146-1L) for 2-4 days. Once stained, embryos were mounted and imaged with a Skyscan 1172 microCT with the following parameters: 100 kV, 100 μA, Al 0.5 mm filter, 1825 ms exposure, 360-degree rotation, 0.3 degree rotation step, image pixel size: 13.49 μm. Raw scan data were reconstructed using NRecon software as described above. Segmentation and 3D renderings were generated using ITK Snap software.

PIXImus Densitometry

PIXImus scans (PIXImus, LUNAR, Madison, WI) were conducted to collect skeletal and body composition data, including Bone Mineral Density (aBMD, g/cm2), Bone Mineral Content (BMC,g), body mass (g), lean mass (g), fat mass (g), and % fat mass, were completed on groups of 6 male and 6 female 12-week old mutant and control mice. The skulls and bodies were scanned separately to provide independent data on skull aBMD and BMC and body aBMD and BMC. The PIXImus small animal densitometer (DEXA) has a resolution of 0.18 x 0.18 mm pixels and is equipped with software version 1.46.

Embryonic skeletal staining

E18.5 embryos were stained with alcian blue and alizarin red as follows: Embryos were fixed in 100% EtOH for 24 hours at room temperature and then 100% acetone for 24 hours at room temperature. Embryos were stained for 3 days at 37°C (1 volume 0.3% Alcian Blue, 1 volume 0.1% Alizarin Red, 1 volume Glacial Acetic Acid, 17 volumes 70% EtOH), rinsed with ddH_2O, transferred into 1% KOH to incubate at room temperature for 3 hours, and then incubated overnight in fresh 1% KOH. Embryos were washed (24 hours each) in 20% glycerol/1% KOH, 50% glycerol/1% KOH, and 80% glycerol/1% KOH, and imaged in an 80% glycerol/1% KOH solution at room temperature.

Histology

Embryos were dissected and fixed in 4% Paraformaldehyde overnight at 4°C. For histology and immunohistochemistry, embryos were washed in PBS, dehydrated through an ethanol series and embedded in paraffin. Five-micron coronal sections through the eye were affixed to Superfrost+ slides (Fisher), dewaxed and hydrated prior to staining with Hematoxylin and Eosin (H&E).

Whole mount in situ hybridization

Embryo processing for whole mount *in situ* hybridization and immunostaining were performed using standard protocols as described in Allen et al. 2007. Probes were gifts from Dr. Thomas Gridley or were generated via RT-PCR from stage-appropriate embryonic cDNA.

Results

Phenotypic characterization and cloning of the Lse mutation

The low-set ears (*Lse*) mouse mutant displays malpositioned and malformed external ear structures that are ventrally shifted relative to littermate controls (Theiler and Sweet, 1986) (Figure 1a,b). *Lse* mice were first identified as a spontaneous mutant on the shaker short-tail J line of mice and exhibit a dominant inheritance pattern. Homozygous adult animals were not found and were therefore presumed to be either embryonic lethal or as rare individuals that were indistinguishable from the heterozygotes. *Lse* affected animals also present with slight bulging of the eyes but live a normal lifespan when maintained on a mixed C57BL/6J;C3H/FeJ F1 genetic background. DEXA analysis of *Lse/+* and WT mice (6 males and 6 females from each genotype) revealed no significant differences in whole body composition, apart from lower body weight for both males and females (Supplementary Figure 1a; Supplementary Table 1). We occasionally observed significantly runted *Lse* animals and individuals with more severe eye abnormalities consistent with dry eye syndrome (keratoconjunctivitis sicca). Skulls from *Lse/+* and WT were analyzed using microCT, revealing two bony differences in the otic region including a hypoplastic paraoccipital process in 9 of 11 heterozygotes and an altered shape of the bulla (Figure 1c,d), the latter consistent with the abnormal orientation of the tympanic ring in the embryonic skeletal stainings. Of note, a hypoplastic paraoccipital process, the attachment site for the digastric muscle, was also reported in *dumbo* rat and mouse mutants which are characterized by large pinnae (Rosin et al., 2016). The hyoid bone in *Lse*/+ mice was also notably abnormal (Supplementary Figure 2). The retrotympanic process (rtp) also tended to be thicker in *Lse*/+ mutants versus control littermates. However, there was variability in thickness even in controls.

Given the malpositioning of the external ear structure, we tested auditory function in mutant animals and littermate controls using auditory brain response (ABR) at 8 weeks and 6 months of age. At 8 weeks the *Lse/+* mice threshold responses were indistinguishable from WT controls at all three frequencies (Supplementary Figure 1b). We identified individuals with moderately impaired ABR response at higher frequencies in both mutant and controls at 6 months, consistent with the presence of a known age-related hearing loss susceptibility allele (*Cdh23*^{ahl}) in the C57BL/6J background (Kane et al., 2012), which segregates in the *Lse* colony. In summary, aside from minor features including eye abnormalities, the phenotype of adult *Lse* mice is primarily limited to the morphology and positioning of the external ear.

Positional cloning identified the *D7Nds4* (MGI:94193) marker which consistently segregated with the *Lse* phenotype during previous attempts to clone the *Lse* mutation.

Conventional PCR-Sanger sequencing of the coding sequence of the *Fgf3*, *Fgf4*, and *Fgf1*5 genes tightly linked to this marker revealed no sequence differences versus controls, suggesting a non-coding or structural etiology. A custom Agilent capture array was designed against the distal end of Chr 7, encompassing 5Mb of sequence centered on D7Nds4. Illumina sequencing of the captured region revealed no coding changes, but a clear increase in read depth across a 148kb interval that includes *Fgf3*, *Fgf4*, and the first exon of *Ano1*, which suggested a duplication (Figure 1e). These findings were independently confirmed by Array CGH performed in parallel (data not shown). At each end of the duplicated interval (Chr7:144,718,321-144,866,450; GRCm38/mm10), we identified read mate-pairs that mapped to the opposite end of the interval and unmapped pairs that included hybrid reads spanning the duplication breakpoint (Figure 1f) which showed a 5-bp insertion accompanying the duplication event. The breakpoint was confirmed by PCR-Sanger sequencing (Figure 1g), and via ddPCR using a breakpoint-spanning probe which differentiated between WT, *Lse/+*, and *Lse/Lse* genotypes (Figure 1h). In addition, ddPCR showed the expected copy number increase of *Fgf3* and *Fgf4* in *Lse/+*, and *Lse/Lse* samples, which confirmed duplication of this region. (Figure 1i,j).

The low set ear phenotype is first visible at E13.5 (Theiler and Sweet, 1986) and is apparent throughout development. In *Lse/+* mutants, the pinnae are ventrally shifted from the developing tragus and a furrow appears near the fossa angularis, which is derived from the first branchial cleft. With the discovery of the mutation structure and the development of a genotyping assay, we performed timed matings of *Lse/+* animals to examine the phenotypes of both *Lse/+* and *Lse/Lse* embryos at E14.5 and E17.5. As shown in Figure 2, the ventrally shifted external ear is visible in both mutant genotypes, with *Lse/Ls*e embryos displaying reduced pinna development. Homozygotes also showed forelimb and hindlimb polydactyly (Figure 2f, arrowhead). At E17.5, homozygous embryos had a cleft secondary palate identified by gross inspection and by iodine-contrast microCT (Dickinson et al., 2016) (Figure 2h), which explains the perinatal lethality of these mice. The eyes protrude in both heterozygous and homozygous embryos (Figure 2h), consistent with the observed phenotype in adult mice. Histological sections of E14.5 *Lse/+* embryos revealed an abnormally thick corneal epithelium that displayed a disorganized stellate morphology. The normal space between the cornea and the lens which will develop into the anterior chamber was also reduced in mutants (Supplementary Figure 3). Notably, this phenotype is similar to that observed in a transgenic line where *Fgf3* is overexpressed using a lens-specific promoter (Robinson et al., 1998), consistent with the duplication of the *Fgf3* gene.

We performed skeletal preparations of WT, *Lse/+* and *Lse/Lse* E18.5 embryos (Figure 3) to further characterize the phenotypes observed in the gross morphology and microCT scans. Heterozygous embryos showed a slightly hypoplastic palatal process of the palatine bone, as well as a ventrally shifted and slightly smaller tympanic ring (Figure 3), consistent with the adult skeletal observations. Confirming our microCT findings, cleft palate was observed in *Lse/Lse* samples revealing the vomer and an extremely hypomorphic and anteriorly shifted tympanic ring (Figure 3a). Analysis of the limbs showed postaxial polydactyly in *Lse/Lse* mutants (Figure 3b).

Increased and ectopic expression of Fgf3 and Fgf4 in Lse embryos

To determine whether the duplication of complete coding sequences of both *Fgf3* and *Fgf4* resulted in detectable differences in levels or spatial patterns of expression, we used whole mount *in situ* hybridization (WISH) to compare the expression of these genes between wildtype, *Lse/+*, and *Lse/Lse* embryos. We examined the expression patterns of *Fgf3* and *Fgf4* at E10.5 when initial patterning of the pharyngeal pouch elements that will become the external ear occurs. In WT embryos at E10.5, *Fgf3* expression was low and restricted to the otic vesicle even after prolonged staining time (Figure 4a). In contrast, while similar levels of expression in the otic vesicle were evident, we observed an ectopic domain of expression in the second branchial arch of *Lse/+* embryos (Figure 4b). Additionally, we observed robust ectopic expression in the developing urogenital ridge (UGR) and expression adjacent to the forelimb bud. In *Lse/Lse* embryos, expression was observed in the same domains as *Lse/+* embryos, but at much higher levels (Figure 4c). The increased expression of *Fgf3* appeared to be nonlinear with respect to copy number, which suggests a loss of normal regulation in addition to the increased number of copies.

Expression of *Fgf4* in both mutant genotypes was similar to controls at E10.5 (Figure 4d–f). At E9.5, *Fgf4* is normally expressed on the rostral aspect of the second and third branchial arches (corresponding to the caudal aspect of the first and second pharyngeal pouches), with a small domain of expression on the fourth arch. In both *Lse/+* and *Lse/Lse* embryos, expression levels of *Fgf4* were similar to controls (Figure 4g–i). However, we observed paired domains of ectopic expression closer to the ventral midline adjacent to the third and fourth arches in mutants compared to controls (Figure 4g'–i'). Taken together, these data show that the *Lse* duplication also results in ectopic expression of *Fgf3* and *Fgf4* and nonlinear overexpression of *Fgf3* in mutants and suggest a complex disruption of normal regulation related to the increased copy number.

Given the increase in *Fgf3* expression in the branchial arches, we next asked whether this would lead to increased FGF signaling via engagement of FGF receptors and signal propagation. Sprouty (*Spry*) is an evolutionarily conserved FGF-responsive intracellular inhibitor of the FGF receptor tyrosine kinase (RTK) pathway and thus serves as a feedback antagonist of FGF signaling (Welsh et al., 2007). FGF pathway activity also induces members of the *Etv* family of transcription factors, including *Etv1*, *Etv4*, and *Etv5*. Compared to control embryos, *in situ* hybridization for *Spry2* and *Etv5* at E10.5 revealed a clear upregulation in the domain of ectopic *Fgf3* expression in the branchial arches of *Lse* mutant embryos versus controls, with a lower degree of upregulation observed in the UGR (Figure 5). These results confirm that increased/ectopic expression of *Fgf3* observed in *Lse* mutants leads to increased FGF signaling in the same locations.

To explore how increased expression of *Fgf3* would affect the position of external ear development, we examined the expression patterns of genes known to regulate positioning of the external ear. *Gsc* and *HoxA2* regulate development of the tympanic ring, which interacts with the developing EAM (Gendron-Maguire et al., 1993; Rivera-Perez et al., 1999). While *Gsc* was slightly reduced in the first pharyngeal cleft in Lse/+ embryos at E10.5, *HoxA2* expression was unaffected (Supplemental Figure 4). Similarly, expression of *Fgf8*, which is required for proper branchial arch patterning and cooperates with *Fgf3* in otic

development, was similar to controls. We next examined the expression of *Dlx* gene family members which are markers of dorsal-ventral patterning. *Dlx2* has the largest expression domain.*Dlx5*, which partially overlaps *Dlx2*, is restricted to the distal (ventral) part of the first arch. *Dlx3* overlaps only the most dorsal part of the *Dlx2* and *Dlx5* domains (Khatri et al., 2014). Whole mount *in situ* hybridization showed no difference in *Dlx2* and *Dlx3* expression patterns (Supplementary Figure 4). Although generally similar, we observed a subtle, but consistent caudal expansion of the *Dlx5* expression domain in *Lse +/−* versus control embryos (Supplementary Figure 4 **e,f**). These data suggest overexpression of *Fgf3* and *Fgf4* in *Lse* mutants does not lead to major patterning changes in developing branchial arches.

Genetic interaction with Twist1

Although patients with11q duplication, which includes *FGF3* and *FGF4*, frequently present with cognitive impairment, ear abnormalities, heart defects, and craniosynostosis, we did not observe suture fusion defects in *Lse/+* mice. Dysregulation of FGF signaling, including mutations in FGF receptors, is known to result in human diseases including craniosynostosis and other skeletal abnormalities (Melville et al., 2010). We asked whether a sensitized background could reveal a skull development or suture abnormality by crossing *Lse* mutants to *Twist1 +/−* mice, which display partially penetrant fusion of the coronal sutures and provide a model for a specific form of craniosynostosis (Bourgeois et al., 1998; Carver et al., 2002; el Ghouzzi et al., 1997). Previous studies showed a functional link between *Twist1* and FGF signaling in the developing sutures (Connerney et al., 2008). Crosses between Lse/+ and Twist1 +/− animals yielded no compound heterozygous animals at wean, which suggested a genetic interaction that compromised viability. Iodine-contrast microCT analysis of E18.5 double heterozygote (*Lse/+; Twist1 +/−*) embryos show the expected low set ear phenotype as well as the known *Twist1 +/−* hindlimb polydactyly phenotype (Chen and Behringer, 1995) (Figure 6a). In P0 litters *Lse/+ Twist1 +/−* embryos had air-filled, swollen abdomens with no milk spot compared to WT littermates (Figure 6b). These phenotypes frequently appear in pups with cleft secondary palate. Although skeletal preparations did not reveal a cleft palate in the *Lse/+;Twist1 +/−* embryos, an apparent posterior cleft was observed in E18.5 microCT scans (Figure 6c). We hypothesized the posterior cleft was an epiglottal soft tissue cleft and confirmed this phenotype by gross inspection of the posterior soft palate (Figure 6d). Together, these data demonstrate a novel genetic interaction between *Twist1* and *Fgf3/4* in the posterior secondary palate.

Discussion

Despite the prevalence of complex syndromes caused by structural variation (SV), including duplications, animal models bearing homologous lesions are lacking. We determined the *Lse* phenotype is caused by a 148kb duplication on chromosome 7 which covers the complete coding sequences of *Fgf3* and *Fgf4* and the first exon of *Ano1*. In the rare human 11q Duplication Syndrome, the size of the duplication varies, but typically includes the *FGF3* and *FGF4* genes. Patient phenotypes include craniosynostosis, heart defects, cognitive impairment, and craniofacial abnormalities including ear abnormalities (Yelavarthi and Zunich, 2004; Zarate et al., 2007). Of ten patients with an 11q duplication, five have

duplications overlapping 11q13.3 where *FGF3* and *FGF4* are found and four of those patients have ear abnormalities, including one case which specified low set ears. The *Lse* mouse may provide a model for 11q duplications to further interrogate how different regions of 11q might affect specific phenotypes.

Fgf3 plays a key role in inner ear development. *Fgf3* signaling in the hindbrain is necessary for proper development of the otic vesicle. In $Fgf3^{-/-}$ embryos, the otic vesicle is smaller and in $Fgf3^{-/-}$; $Fgf10^{+/-}$ embryos, it is more ventrally located than in controls (Wright and Mansour, 2003). Although we did not observe major changes in *Fgf3* expression in the otic vesicle compared to the massive upregulation of expression in the branchial arches and UGR, a subtle increase which corelated with gene dosage was noted. This is consistent with our finding that *Lse* mice hear normally indicating correct development of the cochlea and adjacent sound conduction structures. Because the external ear structures derive from the first and second branchial arches, we explored the effect of the *Lse* duplication on the expression of genes linked to abnormal external ear or EAM development, but found no clear alterations in their expression. Additional studies will be required to identify the targets of *Fgf3/4* signaling which ultimately explain the abnormal morphology of the *Lse* model.

Given the diverse roles of FGFs in mammalian development (Brewer et al., 2016; Ornitz and Itoh, 2015), the limited severity of the morphological phenotypes in the *Lse* mutants is unexpected. This could reflect the fact that overexpression is observed in discrete domains and suggests that this overexpression, despite appearing to be non-linear with respect to copy number, is constrained by the normal regulatory architecture of the locus. In addition, constraint imposed by the affinity of FGF ligands for specific receptors could limit the impact of overexpression to domains where *Fgf3*/*4* would activate signaling. We found that in the branchial arches and UGR that FGF signaling was activated by the increased expression of target genes *Etv5* and *Spry2*. Our phenotypes are consistent with other published models of *Fgf3* overexpression. For example, transgenic mice with ectopic *Fgf3* expression in the lens display dysmorphology of the retinal and corneal tissues and bulging of the eye with the most severe case presenting with a corneal rupture at birth (Robinson et al., 1998). The corneal phenotype in this transgenic model, which includes disorganized corneal epithelial cells and loss of the normal anterior chamber, is consistent with the bulging eyes and histology in *Lse* embryos. Moreover, the Bulgy-eye (*Bey*) (Carlton et al., 1998) mouse line was generated via retroviral insertion into the intragenic region between *Fgf3* and *Fgf4*, which resulted in upregulation of both genes.

Because some 11q duplication patient phenotypes include craniosynostosis, and because of the known role of overactive FGF signaling in the etiology of this clinical phenotype (e.g. Apert syndrome) (Naski et al., 1996; Wilkie et al., 1995), we assessed whether *Lse* mice showed evidence of abnormal suture development. However, the skulls of adult *Lse*/+ mice have normal sutures, while the perinatal lethality of *Lse*/*Lse* pups precluded examination of premature suture fusion. Our attempt to sensitize the background using *Twist1* was confounded by the discovery of a novel genetic interaction between *Fgf3/4* overexpression and *Twist1*, resulting in unique soft palate clefting phenotype. Although there are no studies to our knowledge that demonstrate the interaction of *Twist1* with FGF signaling in palate development, it is notable that both Apert Syndrome (OMIM 101200), caused by activating

mutations in *FGFR2*, and Saethre-Chotzen syndrome (OMIM 101400), caused by *Twist1* or *FGFR2* mutations, include patients with cleft palate. The *Lse* model could serve both as a useful model for 11q duplication syndrome, and as a tool to examine the mechanisms of *Twist1* and FGF signaling during secondary palate development.

Supplementary Material

Refer to Web version on PubMed Central for supplementary material.

Acknowledgements

The authors thank the following for their assistance, expertise and/or helpful feedback on the manuscript: Bo Chang, Norm Hawes, Michelle Curtain, and Kevin Peterson. This work was supported by NIH grants OD021325 (L.G.R. and D.E.B), EY015073 (L.R.D.), DE020052 (S.A.M. and L.R.D.)

References cited

Arnold JS, Braunstein EM, Ohyama T, Groves AK, Adams JC, Brown MC, Morrow BE, 2006. Tissue-specific roles of Tbx1 in the development of the outer, middle and inner ear, defective in 22q11DS patients. Hum Mol Genet 15, 1629–1639. [PubMed: 16600992]

Bourgeois P, Bolcato-Bellemin AL, Danse JM, Bloch-Zupan A, Yoshiba K, Stoetzel C, Perrin-Schmitt F, 1998. The variable expressivity and incomplete penetrance of the twist-null heterozygous mouse phenotype resemble those of human Saethre-Chotzen syndrome. Hum Mol Genet 7, 945–957. [PubMed: 9580658]

Brewer JR, Mazot P, Soriano P, 2016. Genetic insights into the mechanisms of Fgf signaling. Genes Dev 30, 751–771. [PubMed: 27036966]

Carlton MB, Colledge WH, Evans MJ, 1998. Crouzon-like craniofacial dysmorphology in the mouse is caused by an insertional mutation at the Fgf3/Fgf4 locus. Dev Dyn 212, 242–249. [PubMed: 9626498]

Carver EA, Oram KF, Gridley T, 2002. Craniosynostosis in Twist heterozygous mice: a model for Saethre-Chotzen syndrome. Anat Rec 268, 90–92. [PubMed: 12221714]

Chen ZF, Behringer RR, 1995. twist is required in head mesenchyme for cranial neural tube morphogenesis. Genes Dev 9, 686–699. [PubMed: 7729687]

Connerney J, Andreeva V, Leshem Y, Mercado MA, Dowell K, Yang X, Lindner V, Friesel RE, Spicer DB, 2008. Twist1 homodimers enhance FGF responsiveness of the cranial sutures and promote suture closure. Dev Biol 318, 323–334. [PubMed: 18471809]

Cox TC, Camci ED, Vora S, Luquetti DV, Turner EE, 2014. The genetics of auricular development and malformation: new findings in model systems driving future directions for microtia research. Eur J Med Genet 57, 394–401. [PubMed: 24880027]

Dickinson ME, Flenniken AM, Ji X, Teboul L, Wong MD, White JK, Meehan TF, Weninger WJ, Westerberg H, Adissu H, Baker CN, Bower L, Brown JM, Caddle LB, Chiani F, Clary D, Cleak J, Daly MJ, Denegre JM, Doe B, Dolan ME, Edie SM, Fuchs H, Gailus-Durner V, Galli A, Gambadoro A, Gallegos J, Guo S, Horner NR, Hsu CW, Johnson SJ, Kalaga S, Keith LC, Lanoue L, Lawson TN, Lek M, Mark M, Marschall S, Mason J, McElwee ML, Newbigging S, Nutter LM, Peterson KA, Ramirez-Solis R, Rowland DJ, Ryder E, Samocha KE, Seavitt JR, Selloum M, Szoke-Kovacs Z, Tamura M, Trainor AG, Tudose I, Wakana S, Warren J, Wendling O, West DB, Wong L, Yoshiki A, International Mouse Phenotyping, C., Jackson L, Infrastructure Nationale Phenomin, I.C.d.l.S., Charles River L, Harwell MRC, Toronto Centre for, P., Wellcome Trust Sanger, I., Center RB, MacArthur DG, Tocchini-Valentini GP, Gao X, Flicek P, Bradley A, Skarnes WC, Justice MJ, Parkinson HE, Moore M, Wells S, Braun RE, Svenson KL, de Angelis MH, Herault Y, Mohun T, Mallon AM, Henkelman RM, Brown SD, Adams DJ, Lloyd KC, McKerlie C, Beaudet AL, Bucan M, Murray SA, 2016. High-throughput discovery of novel developmental phenotypes. Nature 537, 508–514. [PubMed: 27626380]

Dixon MJ, 1995. Treacher Collins syndrome. J Med Genet 32, 806–808. [PubMed: 8558560]

el Ghouzzi V, Le Merrer M, Perrin-Schmitt F, Lajeunie E, Benit P, Renier D, Bourgeois P, Bolcato-Bellemin AL, Munnich A, Bonaventure J, 1997. Mutations of the TWIST gene in the Saethre-Chotzen syndrome. Nat Genet 15, 42–46. [PubMed: 8988167]

Fekete DM, 1999. Development of the vertebrate ear: insights from knockouts and mutants. Trends Neurosci 22, 263–269. [PubMed: 10354604]

Fuchs JC, Tucker AS, 2015. Development and Integration of the Ear. Curr Top Dev Biol 115, 213–232. [PubMed: 26589927]

Gendron-Maguire M, Mallo M, Zhang M, Gridley T, 1993. Hoxa-2 mutant mice exhibit homeotic transformation of skeletal elements derived from cranial neural crest. Cell 75, 1317–1331. [PubMed: 7903600]

Grevellec A, Tucker AS, 2010. The pharyngeal pouches and clefts: Development, evolution, structure and derivatives. Semin Cell Dev Biol 21, 325–332. [PubMed: 20144910]

Kane KL, Longo-Guess CM, Gagnon LH, Ding D, Salvi RJ, Johnson KR, 2012. Genetic background effects on age-related hearing loss associated with Cdh23 variants in mice. Hear Res 283, 80–88. [PubMed: 22138310]

Khatri SB, Edlund RK, Groves AK, 2014. Foxi3 is necessary for the induction of the chick otic placode in response to FGF signaling. Dev Biol 391, 158–169. [PubMed: 24780628]

Kohlhase J, Heinrich M, Schubert L, Liebers M, Kispert A, Laccone F, Turnpenny P, Winter RM, Reardon W, 2002. Okihiro syndrome is caused by SALL4 mutations. Hum Mol Genet 11, 2979–2987. [PubMed: 12393809]

Lambert PR, Dodson EE, 1996. Congenital malformations of the external auditory canal. Otolaryngol Clin North Am 29, 741–760. [PubMed: 8893214]

Mahoney Rogers AA, Zhang J, Shim K, 2011. Sprouty1 and Sprouty2 limit both the size of the otic placode and hindbrain Wnt8a by antagonizing FGF signaling. Dev Biol 353, 94–104. [PubMed: 21362415]

Melville H, Wang Y, Taub PJ, Jabs EW, 2010. Genetic basis of potential therapeutic strategies for craniosynostosis. Am J Med Genet A 152A, 3007–3015. [PubMed: 21082653]

Minoux M, Kratochwil CF, Ducret S, Amin S, Kitazawa T, Kurihara H, Bobola N, Vilain N, Rijli FM, 2013. Mouse Hoxa2 mutations provide a model for microtia and auricle duplication. Development 140, 4386–4397. [PubMed: 24067355]

Naski MC, Wang Q, Xu J, Ornitz DM, 1996. Graded activation of fibroblast growth factor receptor 3 by mutations causing achondroplasia and thanatophoric dysplasia. Nat Genet 13, 233–237. [PubMed: 8640234]

Ornitz DM, Itoh N, 2015. The Fibroblast Growth Factor signaling pathway. Wiley Interdiscip Rev Dev Biol 4, 215–266. [PubMed: 25772309]

Rice R, Spencer-Dene B, Connor EC, Gritli-Linde A, McMahon AP, Dickson C, Thesleff I, Rice DP, 2004. Disruption of Fgf10/Fgfr2b-coordinated epithelial-mesenchymal interactions causes cleft palate. J Clin Invest 113, 1692–1700. [PubMed: 15199404]

Rivera-Perez JA, Wakamiya M, Behringer RR, 1999. Goosecoid acts cell autonomously in mesenchyme-derived tissues during craniofacial development. Development 126, 3811–3821. [PubMed: 10433910]

Robinson ML, Ohtaka-Maruyama C, Chan CC, Jamieson S, Dickson C, Overbeek PA, Chepelinsky AB, 1998. Disregulation of ocular morphogenesis by lens-specific expression of FGF-3/int-2 in transgenic mice. Dev Biol 198, 13–31. [PubMed: 9640329]

Rosin JM, Li W, Cox LL, Rolfe SM, Latorre V, Akiyama JA, Visel A, Kuramoto T, Bobola N, Turner EE, Cox TC, 2016. A distal 594 bp ECR specifies Hmx1 expression in pinna and lateral facial morphogenesis and is regulated by the Hox-Pbx-Meis complex. Development 143, 2582–2592. [PubMed: 27287804]

Stanier P, Pauws E, 2012. Development of the lip and palate: FGF signalling. Front Oral Biol 16, 71–80. [PubMed: 22759671]

Tekin M, Ozturkmen Akay H, Fitoz S, Birnbaum S, Cengiz FB, Sennaroglu L, Incesulu A, Yuksel Konuk EB, Hasanefendioglu Bayrak A, Senturk S, Cebeci I, Utine GE, Tuncbilek E, Nance WE, Duman D, 2008. Homozygous FGF3 mutations result in congenital deafness with inner ear agenesis, microtia, and microdontia. Clin Genet 73, 554–565. [PubMed: 18435799]

Theiler K, Sweet HO, 1986. Low set ears (Lse), a new mutation of the house mouse. Anat Embryol (Berl) 175, 241–246. [PubMed: 3103484]

Tingaud-Sequeira A, Trimouille A, Sagardoy T, Lacombe D, Rooryck C, 2022. Oculo-auriculo-vertebral spectrum: new genes and literature review on a complex disease. J Med Genet 59, 417–427. [PubMed: 35110414]

Turner N, Grose R, 2010. Fibroblast growth factor signalling: from development to cancer. Nat Rev Cancer 10, 116–129. [PubMed: 20094046]

Welsh IC, Hagge-Greenberg A, O'Brien TP, 2007. A dosage-dependent role for Spry2 in growth and patterning during palate development. Mech Dev 124, 746–761. [PubMed: 17693063]

Wilkie AO, Slaney SF, Oldridge M, Poole MD, Ashworth GJ, Hockley AD, Hayward RD, David DJ, Pulleyn LJ, Rutland P, et al. , 1995. Apert syndrome results from localized mutations of FGFR2 and is allelic with Crouzon syndrome. Nat Genet 9, 165–172. [PubMed: 7719344]

Wilkinson DG, Peters G, Dickson C, McMahon AP, 1988. Expression of the FGF-related proto-oncogene int-2 during gastrulation and neurulation in the mouse. EMBO J 7, 691–695. [PubMed: 3293998]

Wong MD, Spring S, Henkelman RM, 2013. Structural stabilization of tissue for embryo phenotyping using micro-CT with iodine staining. PLoS One 8, e84321. [PubMed: 24386367]

Wright TJ, Mansour SL, 2003. Fgf3 and Fgf10 are required for mouse otic placode induction. Development 130, 3379–3390. [PubMed: 12810586]

Yelavarthi KK, Zunich J, 2004. Familial interstitial duplication of 11q; partial trisomy (11)(q13.5q21). Am J Med Genet A 126A, 423–426. [PubMed: 15098242]

Zarate YA, Kogan JM, Schorry EK, Smolarek TA, Hopkin RJ, 2007. A new case of de novo 11q duplication in a patient with normal development and intelligence and review of the literature. Am J Med Genet A 143A, 265–270. [PubMed: 17219392]

Zhang Y, Fons JM, Hajihosseini MK, Zhang T, Tucker AS, 2020. An Essential Requirement for Fgf10 in Pinna Extension Sheds Light on Auricle Defects in LADD Syndrome. Front Cell Dev Biol 8, 609643. [PubMed: 33363172]

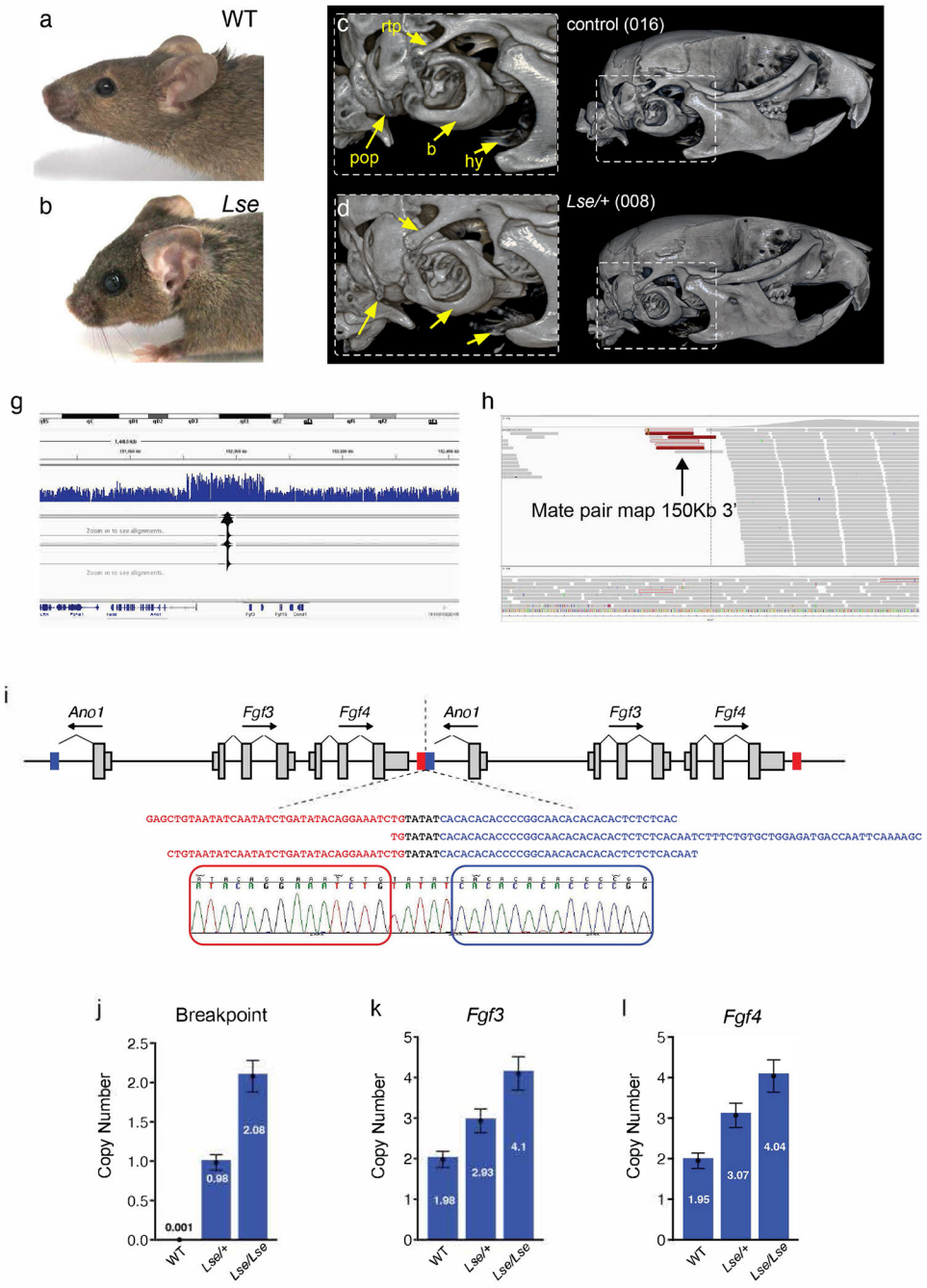

Figure 1: The low set ears (*Lse*) mouse mutant is caused by a tandem duplication which includes *Fgf3* and *Fgf4*.

(**a,b**) *Lse* mutant mice display abnormal external ear morphology, including both the position and shape of the external auditory meatus (EAM) and the overall appearance of the pinnae. Mutant mice also display variably penetrant bulging eyes. (**c,d**) MicroCT scans of adult *Lse/+* and WT skulls revealed a number of subtle bony anomalies, including altered morphology of the bulla (b), hypoplasia of the paraoccipital process (pop), and abnormal morphology of hyoid bone (hy). The retrotympanic process (rtp) appeared to be thicker

in heterozygotes than controls, although ~40% of controls had processes of comparable thickness. (**e**) IGV visualization of array-captured sequencing of the region around the D7Nds4 marker showing the increase in apparent read number mapping to the region, which suggests a copy number variation. (**f**) IGV visualization of individual sequencing reads with mate pairs that map to the 3' end of the 148Kb interval. (**g**) Reconstruction of the duplicated region, color coded to indicate sequences at the 5' (blue) and 3' (red) of the interval. Breakpoint reads which define the tail-head fusion were identified from unmapped mate pairs (gray with red outline in **f**), and confirmed by Sanger sequencing. (**h**) A digital droplet PCR (ddPCR) breakpoint assay was used to genotype the *Fgf3/4* duplication, and the duplication was confirmed by ddPCR copy number assessment of the *Fgf3* **(i)** and *Fgf4* (**j**) genes in WT, *Lse*/+, and *Lse*/*Lse* embryos.

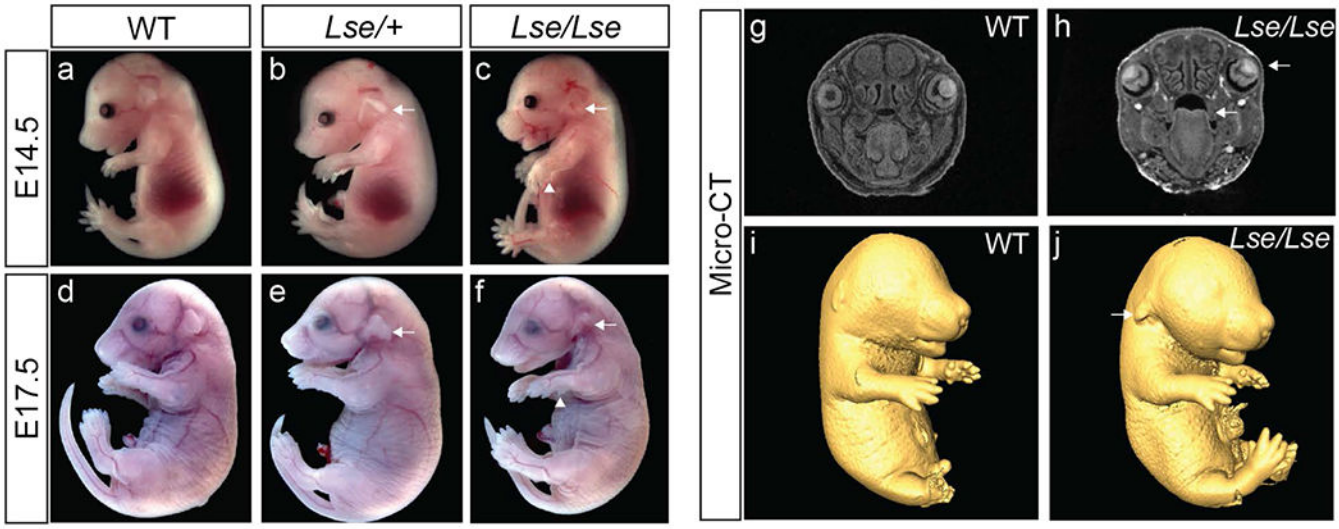

Figure 2: Gross morphology of *Lse* mutants.

Appearance of WT, *Lse*/+, and *Lse*/*Lse* embryos at E14.5 (**a-c**) and E17.5 (**d-f**). The malpositioned external ear is evident in both mutant genotypes at each stage (arrows) and polydactyly is noted in *Lse*/*Lse* embryos (arrowheads in **c** and **f**). (**g,h**) MicroCT imaging reveals cleft secondary palate and bulging eyes in *Lse*/*Lse* mutants and surface renderings (**i, j**) illustrate the abnormal shape of the pinnae in mutants.

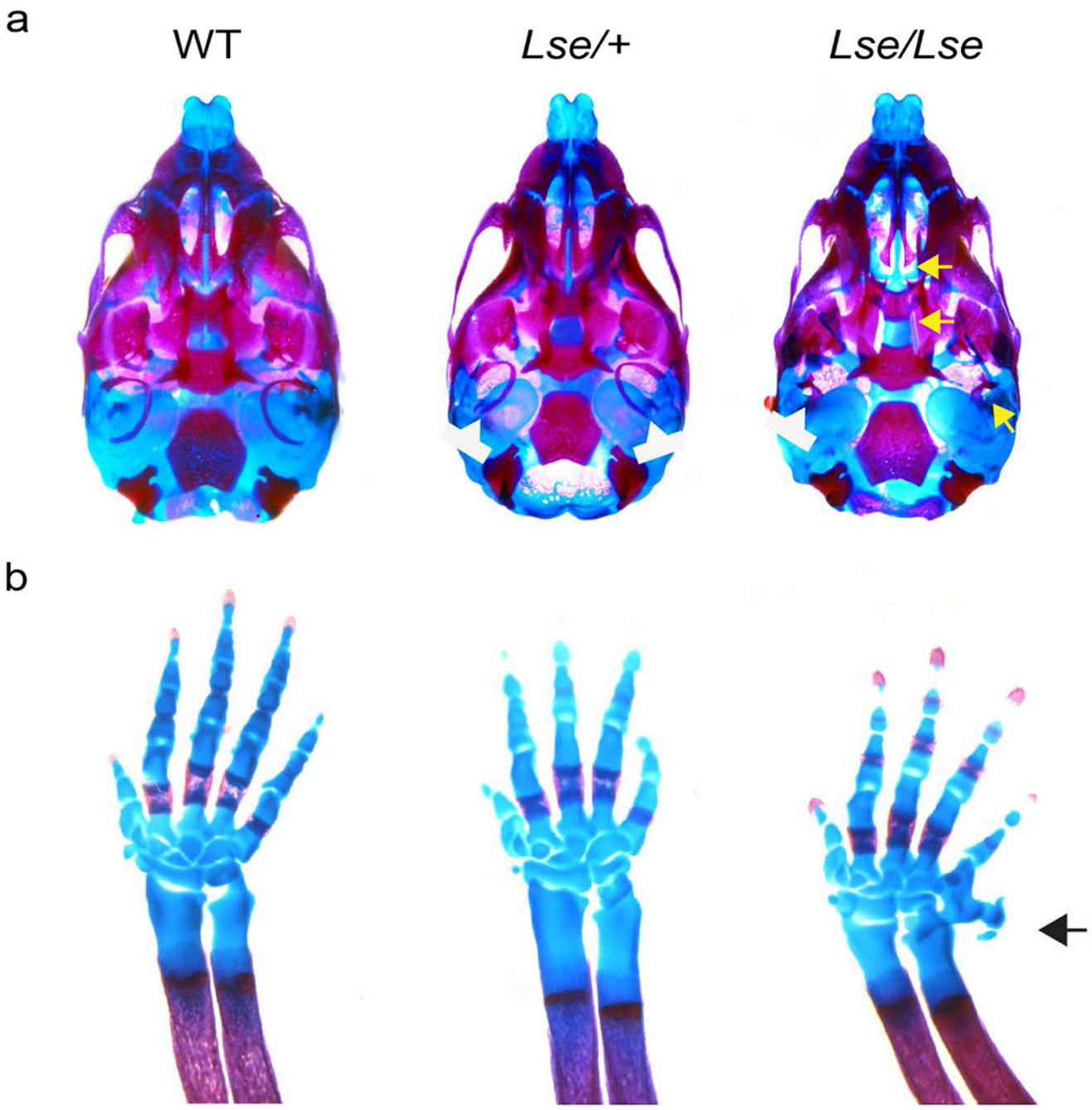

Figure 3: Skeletal abnormalities in *Lse* embryos.

(**a**) Alizarin red/alcian blue staining at E18.5 reveal minor abnormalities in the palatal process and tympanic ring in *Lse*/+ embryos, while *Lse*/*Lse* skulls showed cleft secondary palate and a hypomorphic tympanic ring remnant (yellow arrows). (**b**) Staining of limbs show postaxial polydactyly in *Lse*/*Lse* mutants only (arrow).

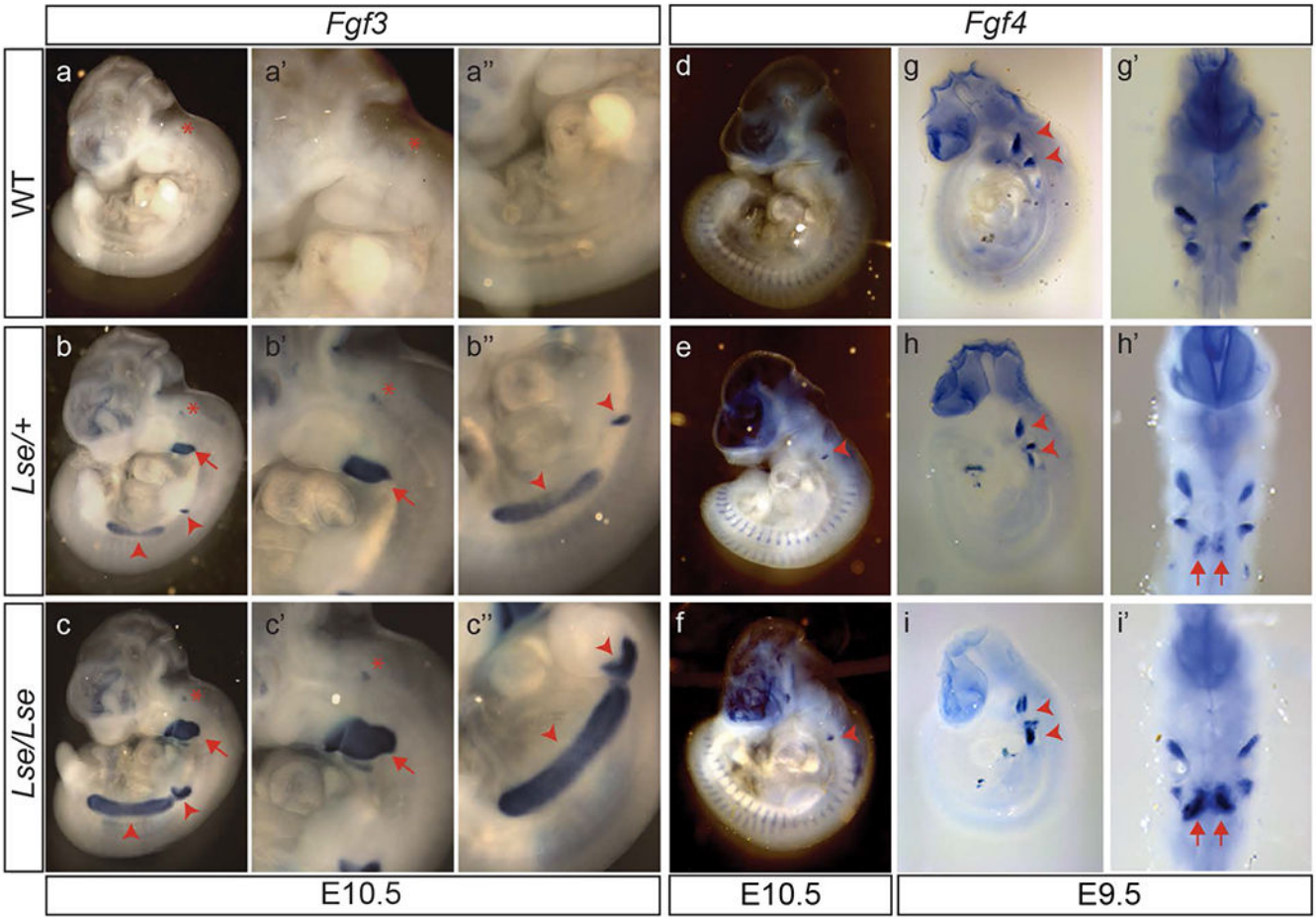

Figure 4: Increased and ectopic expression of *Fgf3* and *Fgf4* in *Lse* mutant embryos.

Whole mount in situ hybridization for *Fgf3* (**a-c**) at E10.5 reveals highly increased expression levels in the second branchial arch in *Lse*/+ embryos (arrow in **b** and **b'**), with ectopic expression in the urogenital ridge and adjacent to the forelimb (arrowheads **b** and **b''**). *Lse*/*Lse* embryos show a similar pattern but with higher expression levels (**c, c', c''**), with some expansion of the expression domain into the first branchial arch. Otocyst expression is indicated by *. (**d-f**) *Fgf4* expression at E10.5 shows a modest increase in expression in the caudal aspect of the second arch with similar levels in both *Lse*/+ and *Lse*/*Lse* embryos. At E9.5 (**g-i**), similar levels of *Fgf4* expression are seen in mutants and controls in the arches (arrowheads), but an additional domain of ventral expression is observed in both mutants, with higher levels in *Lse*/*Lse* embryos (arrows in **h**' and **i**').

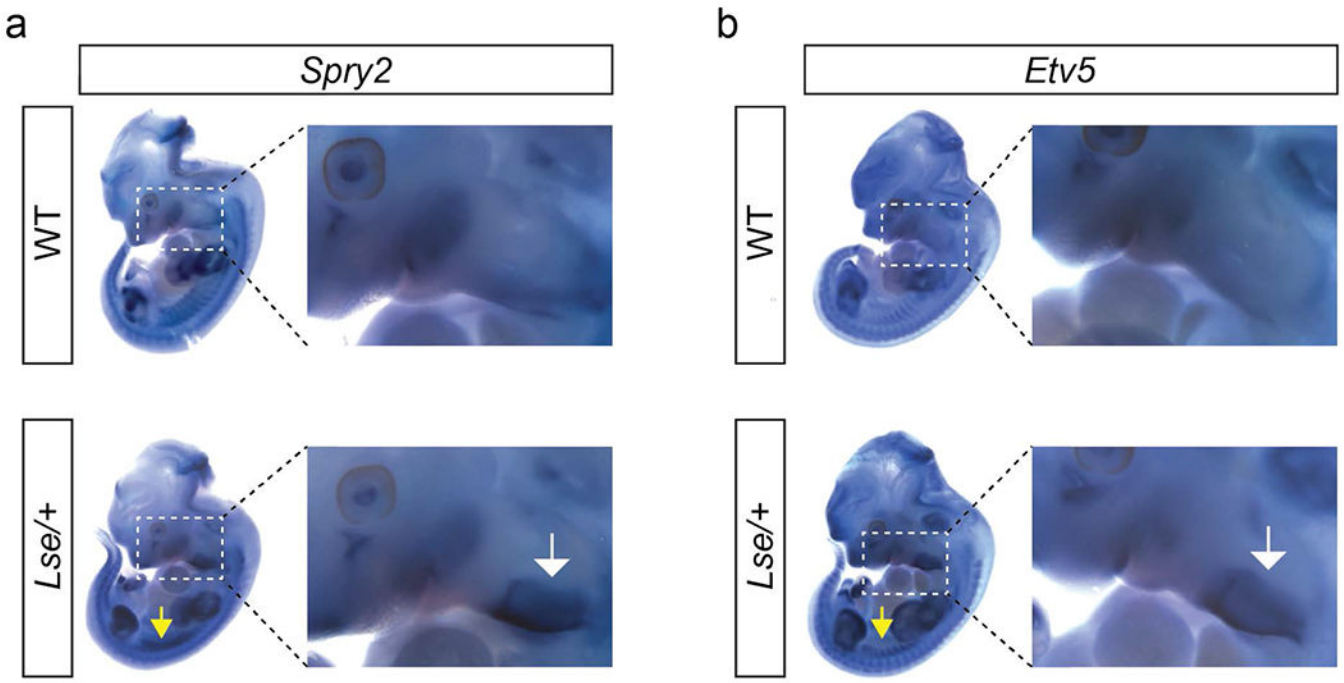

Figure 5: The *Lse* duplication leads to increased FGF signaling.

Whole mount *in situ* hybridization reveals increased expression of FGF pathway targets *Spry2* (**a**) and *Etv5* (**b**) in *Lse*/+ mutants versus controls. This is observed in domains which overlap expanded *Fgf3* expression, including the branchial arches (inset, white arrow), and the urogenital ridge (yellow arrow).

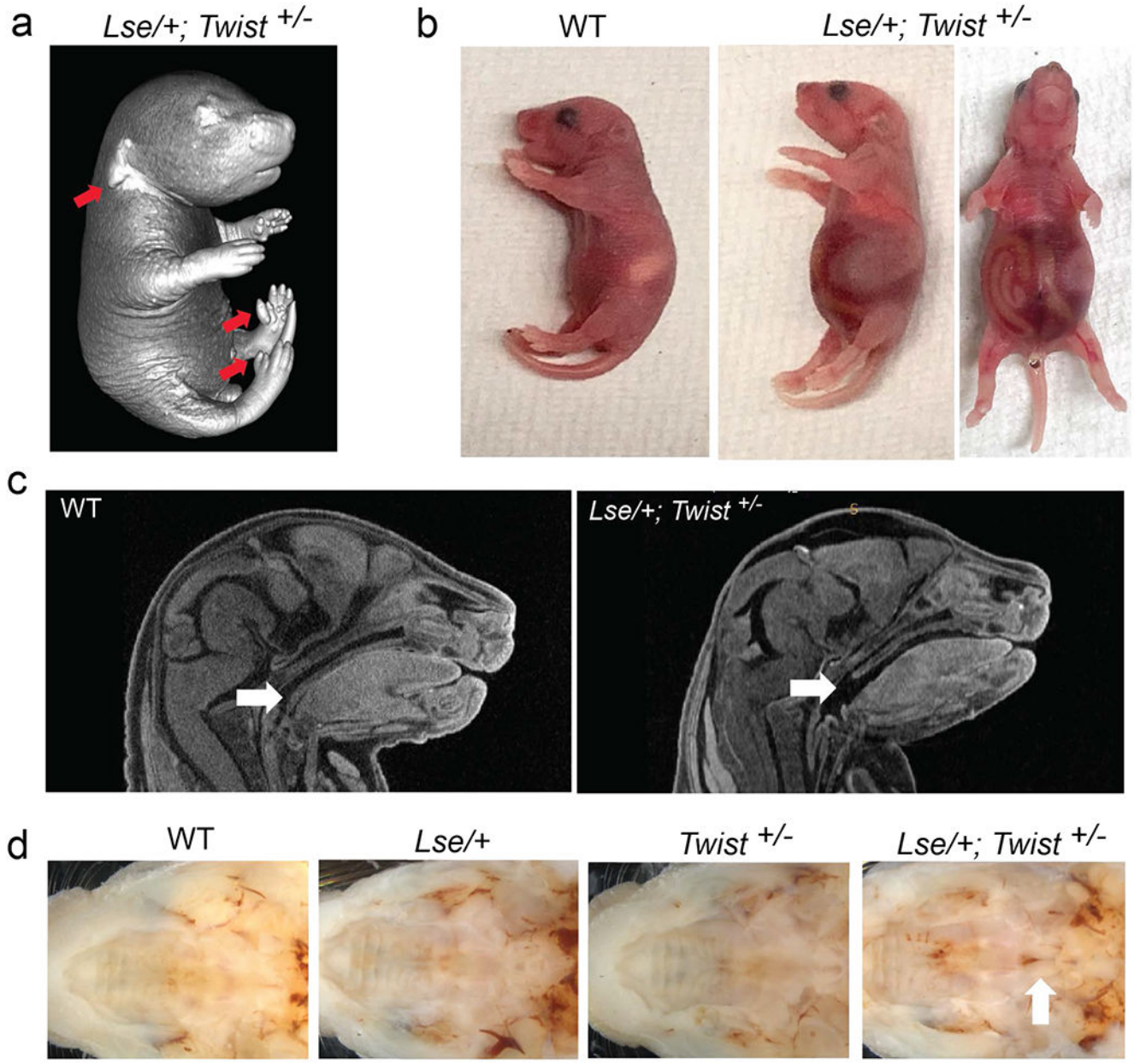

Figure 6: Genetic interaction between *Lse* and *Twist1*.

(**a**) Surface rendering of a microCT scan of a *Lse*/+; *Twist* +/− E18.5 embryo showing the expected low set ear phenotype and polydactyly on both limbs (red arrows). (**b**) Gross appearance of *Lse*/+;*Twist*+/− neonates with distention of the abdomen and lack of a milk spot, consistent with ingestion of air while feeding. (**c**) Sagittal sections of a microCT scan showing apparent posterior, soft-tissue palate cleft, which was confirmed in gross dissections (**d**).